

# Evidence of Memory Effects in the Dynamics of Two-Level System Defect Ensembles Using Broadband, Cryogenic Transient Dielectric Spectroscopy

Qianxu Wang,<sup>1,2</sup> Sara Magdalena Gómez,<sup>1,2</sup> Juan S. Salcedo-Gallo,<sup>2</sup> Roy Leibovitz,<sup>2</sup> Jake Freeman,<sup>3,2</sup> Simon A. Agnew,<sup>2</sup> Salil Bedkhal,<sup>2</sup> William J. Scheideler,<sup>2</sup> and Mattias Fitzpatrick<sup>1,2,\*</sup>

<sup>1</sup>Department of Physics and Astronomy, Dartmouth College, 6127 Wilder Laboratory, Hanover, New Hampshire 03755, USA

<sup>2</sup>Thayer School of Engineering, Dartmouth College, 15 Thayer Drive, Hanover, New Hampshire 03755, USA

<sup>3</sup>Department of Physics, Middlebury College, Middlebury, Vermont 05753, USA

(Dated: November 20, 2025)

Two-level system (TLS) defects in dielectrics cause decoherence in superconducting circuits, yet their origin, frequency distribution, and dipole moments remain poorly understood. Current probes, primarily based on qubits or resonators, require complex fabrication and measure defects only within narrow frequency bands and limited mode volumes, restricting insight into TLS behavior in isolated materials and interfaces. We introduce Broadband Cryogenic Transient Dielectric Spectroscopy (BCTDS), a broadband 3D waveguide technique that enables probing of TLS ensembles at cryogenic temperatures. Complementary to the dielectric dipper method, this approach probes a broader spectrum and reveals interference of drive-induced sidebands in TLS ensembles. The broadband, power-tunable nature of BCTDS makes it well suited for studying dressed-state physics in driven TLS ensembles, including multi-photon processes and sideband-resolved dynamics. By analyzing Fourier-transformed time-domain signals, BCTDS reveals eigen-mode frequencies of undriven TLS ensembles through characteristic V-shaped features and uncovers memory effects arising from interactions and broadband excitation. The modular method can be applied throughout device fabrication, informing mitigation strategies and advancing the design of low-loss materials with broad implications for quantum technologies and materials science.

## I. INTRODUCTION

TLS defects are necessary to describe anomalous low-temperature properties of disordered solids, and they play a critical role in limiting the coherence of quantum technologies such as superconducting qubits and resonators. At low temperatures, many amorphous solids exhibit a thermodynamic behavior that deviates significantly from the predictions of Debye theory, which describes the specific heat of crystalline materials as scaling with  $T^3$ . In contrast, experiments in the early 1970s revealed that glassy materials display a nearly linear temperature dependence of the specific heat at cryogenic temperatures [1]. To describe this low temperature behavior, Anderson, Halperin, and Varma [2], and independently Phillips [3], introduced the standard tunneling model, illustrated in Fig. 1(a). The model treats disordered materials as a collection of effective double-well potentials where quantum tunneling can occur. Today, it is widely believed that individual TLS defects are ubiquitous and form an ensemble whose collective low-energy excitations account for the observed linear temperature dependence of the specific heat capacity. Early models treated TLS defects as non-interacting and uniformly distributed in frequency, which sufficed to explain the specific heat capacity measurements. However, studies have shown that TLS defects can interact, leading to spectral diffusion, clustering, and nonlinear loss [4–10].

While the notion of a TLS defect was initially developed to explain the thermodynamic properties of glassy

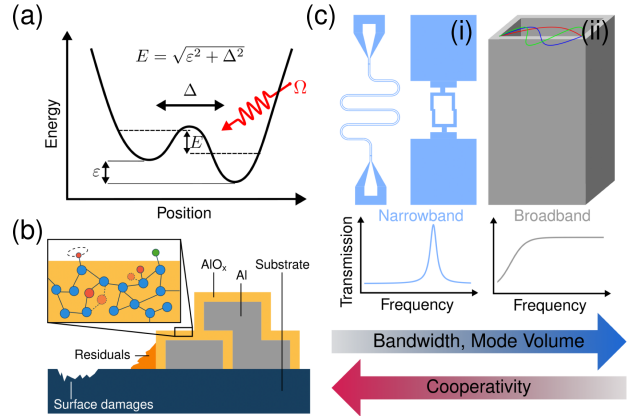


FIG. 1. Overview of TLS defects and how they can be probed. (a) Double-well representation of TLS defects under a drive  $\Omega$ , described by the standard tunneling model. (b) Candidate TLS defects and their likely locations in superconducting circuits. (c) Comparison of traditional TLS defect spectroscopy using 2D qubits and resonators and our proposed broadband 3D waveguide approach. The concept of image (b) is inspired by [11].

materials, such defects have recently regained relevance in solid-state quantum computing technologies. This renewed interest is especially evident in superconducting circuits, which have become a leading platform for quantum computing primarily due to their fast gate times, design flexibility, and compatibility with advanced semiconductor fabrication techniques. However, their decoherence times are relatively short compared to other

\* mattias.w.fitzpatrick@dartmouth.edu

promising quantum technologies, such as neutral atoms, trapped ions, and spin qubits. From measurements of bulk loss tangents [12, 13], and modeling of the Purcell effect [14–16], it has become clear that other sources of loss must be present. Furthermore, measurements of qubit coherence while changing electric field and mechanical strain provide explicit evidence of TLS defects in superconducting circuits [11, 17–20]. Currently, the prevailing understanding is that decoherence in superconducting circuits is dominated by TLS defects on surfaces and interfaces, as illustrated in Fig. 1(b), although their specific atomistic origin remains unclear [21–25].

TLS defects are typically probed via photonic or acoustic resonators [26–30] and qubits [11, 12, 17–19, 31]. These approaches provide high cooperativity but preferentially detect TLS defects with dipole moments aligned with the directly integrated probes, and are restricted to small bandwidths and mode volumes, as depicted in Fig. 1(c). Despite these limitations, several studies have demonstrated the existence of TLS-TLS interactions [19, 32, 33], and non-Markovian dynamics [34, 35], leading to questions about the nature of TLS defect interactions in the absence of strongly coupled probes [36]. In the spirit of the Mollow triplet, our setup enables the observation of dressed-state features in interacting ensembles of TLS defects, where the underlying spectral structure can reflect many-body dynamics rather than single-emitter coherence [37]. Furthermore, our method can be extended to accurately map the frequency and dipole moments of ensembles of TLS defects by employing a polarization-dependent drive. While conventional techniques such as electron spin resonance (ESR) focus on detecting net magnetization changes associated with spin-active defects using narrowband field excitation, BCTDS enables parallel, broadband interrogation of both spin and non-spin defects by directly measuring their transient electromagnetic and dielectric responses.

In addition to their impact on the decoherence of superconducting qubits, TLS defects also influence the fidelity of qubit readout. In particular, TLS defects can manifest in Josephson traveling wave parametric amplifiers (JTWPA), which are crucial for high-fidelity qubit readout due to their quantum-limited amplification and several GHz of bandwidth [38, 39]. However, recent experiments show that high-power pulses can excite long-lived dielectric echoes in JTWPA, which are attributed to ensembles of TLS defects [40, 41]. These echoes impair the readout fidelity of experiments utilizing JTWPA (and likely other parametric amplifiers), motivating careful characterization of the transient dynamics of interacting ensembles of TLS defects.

Here, we propose a modular, non-invasive technique that enables BCTDS of ensembles of TLS defects in isolated materials and devices. Through systematic and longitudinal studies, this technique will provide essential data that will shed light on the atomistic nature of TLS defects and their properties [42]. Such insights will inform the design of the next generation of quantum

hardware from a first-principles understanding of TLS defects, something which was recently highlighted as a pressing need for the superconducting qubit community by the Google Quantum AI hardware team [43].

## II. BROADBAND CRYOGENIC TRANSIENT DIELECTRIC SPECTROSCOPY

### A. Modular, Broadband 3D Microwave Waveguide

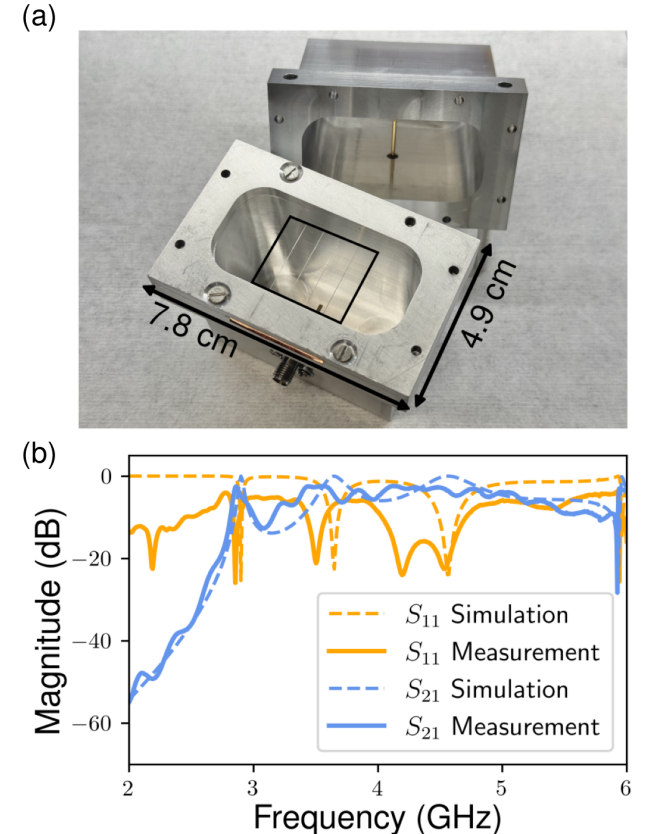


FIG. 2. Broadband waveguide design. (a) Photograph of upper and lower WR-229 to SMA adapter components and clamp with sapphire samples (marked by the black box). These components are assembled to create the closed 3D aluminum waveguide used in this work. (b) HFSS simulated and measured transmission ( $S_{21}$ ) and reflection ( $S_{11}$ ) spectra of the waveguide containing samples at room temperature, demonstrating a waveguide cutoff of around 3 GHz and broadband transmission from 3–6 GHz.

To probe the dielectric response in the microwave frequency domain, we leverage a broadband 3D waveguide, shown in Fig. 2(a). In contrast to qubit and resonator-based probes, this method allows for coupling to ensembles of TLS defects over a broad frequency range. As described in Appendix A, the closed waveguide comprises two WR-229 to coaxial cable adapters joined by a sample clamp. This modular approach allows us to

easily measure samples of different sizes, shapes, and material compositions across a broadband range of 3–6 GHz. The corresponding S-parameter curves are shown in Fig. 2(b). Importantly, these features distinguish our approach from existing narrow-band qubit and resonator-based probes, which require samples to go through a full fabrication cycle, followed by wire bonding and packaging, making it nearly impossible to perform additional material processing and characterization. Furthermore, this constraint makes the development of new fabrication recipes wasteful and inefficient.

### B. Dielectric Response of an Ensemble of TLS Defects

Applying an external time-dependent electric field to dielectric materials induces a polarization that reflects the collective dielectric response. This response is dominated by a distribution of atomic-scale TLS defects at low temperatures, whose energy splittings and coupling strengths vary widely due to structural disorder. Within the linear response regime, the relationship between the applied field and the induced polarization is captured by the dynamical susceptibility of the material, which encodes both in- and out-of-phase components of the ensembles of TLS defects' response. In our experiment, the response can extend beyond the linear regime when the system is influenced by strong, broadband, or pulsed electric fields, making the susceptibility dependent on amplitude, leading to higher-order contributions to the susceptibility. In this context, we use the dynamical susceptibility framework as a conceptual tool to interpret the response, even though saturation and non-linear effects likely play a significant role. After the drive is turned off, the system enters a transient regime, where the energy absorbed by TLS defects begins to dissipate. By monitoring the subsequent time evolution of the polarization-dependent homodyne signal, we perform BCTDS, which reveals signatures of the TLS defects dynamics.

To understand this system, we first consider a single TLS defect characterized by an energy detuning  $\varepsilon_j$  and a tunneling amplitude  $\Delta_j$ , as illustrated in Fig. 1(a). The effective Hamiltonian for the  $j$ -th TLS defect in the position basis  $\{|L\rangle, |R\rangle\}$  can be written as [19]

$$\hat{H}_j = \frac{1}{2} \begin{pmatrix} \varepsilon_j & \Delta_j \\ \Delta_j & -\varepsilon_j \end{pmatrix} = \frac{1}{2} \varepsilon_j \hat{\sigma}_z^{(p,j)} + \frac{1}{2} \Delta_j \hat{\sigma}_x^{(p,j)}, \quad (1)$$

where  $\hat{\sigma}_z^{(p,j)}$  and  $\hat{\sigma}_x^{(p,j)}$  are Pauli matrices in the position basis representing the difference between left and right localized states.

Diagonalizing this Hamiltonian yields the energy eigenstates with eigenenergies

$$E_j = \sqrt{\varepsilon_j^2 + \Delta_j^2}, \quad (2)$$

and defines a mixing angle  $\theta_j$  through

$$\tan \theta_j = \frac{\Delta_j}{\varepsilon_j}. \quad (3)$$

Transforming to this energy eigenbasis, the static Hamiltonian simplifies to

$$\hat{H}_{0,j} = \frac{1}{2} E_j \hat{\sigma}_z^{(j)}, \quad (4)$$

where  $\hat{\sigma}_z^{(j)}$  now acts in the energy eigenbasis.

Next, we introduce the interaction of the ensembles of TLS defects with an external, time-dependent electric field  $\mathbf{E}(t)$ . The coupling occurs via the electric dipole moment  $\mathbf{p}_j$  of the TLS defect [37]. Choosing the dipole moment direction as the quantization axis (here aligned along  $\hat{\mathbf{x}}$ ), the collective polarization operator for an ensemble of  $N$  TLS defects can be defined as

$$\hat{\mathbf{P}} = \sum_{j=1}^N p_j \left( \cos \theta_j \hat{\sigma}_z^{(j)} + \sin \theta_j \hat{\sigma}_x^{(j)} \right) \hat{\mathbf{x}}, \quad (5)$$

where the Pauli operators are in the energy eigenbasis.

The full Hamiltonian, including the interaction with the electric field, is then written as

$$\hat{H}(t) = \sum_{j=1}^N \hat{H}_{0,j} - \hat{\mathbf{P}} \cdot \mathbf{E}(t). \quad (6)$$

In our experimental setup, the electromagnetic field is polarized and can be represented as

$$\mathbf{E}(t) = (E_0 e^{-i\omega_0 t} + E_0^* e^{i\omega_0 t}) \hat{\mathbf{x}}, \quad (7)$$

where  $E_0$  is the complex amplitude and  $\omega_0$  the driving frequency.

This formulation captures the static energy structure of the ensembles of TLS defects and its collective coupling to the external, oscillating electric field. However, in practice, the dynamical response includes additional features such as Stark shifts and nonlinearities [44]. Unlike prior narrow-band experiments that probe TLS defects indirectly using a qubit or resonator, our approach directly drives the entire ensemble of TLS defects. This motivates including the drive term in Eq. 6 within the standard tunneling model.

The interaction in Eq. 6 causes an induced dipole moment with expectation value  $\langle \hat{P}(t) \rangle$ . Assuming that the medium is isotropic and the polarization is parallel to the electric field, we can express the average polarization using the Kubo formula [45]

$$\langle \hat{P}(t) \rangle = \int_{-\infty}^{\infty} dt' \chi(t - t') E(t'), \quad (8)$$

where  $E$  is the amplitude of the electric field, and the susceptibility is given by

$$\chi(t) = i\theta(t)\langle[\hat{P}(t), \hat{P}(0)]\rangle_0, \quad (9)$$

where  $\langle \cdots \rangle_0$  denotes the equilibrium expectation value and  $\theta(t)$  is the Heaviside step function. Note that the Kubo framework introduced here is only a conceptual tool to motivate the spectroscopic technique. The observed transient response in our experiment seems to suggest nonlinear contributions to the susceptibility, and we are likely far from the linear regime. However, we can still proceed by considering the Fourier transform of the induced polarization, which is given by

$$\langle \hat{P}(\omega) \rangle = \chi(\omega)E(\omega), \quad (10)$$

where

$$\chi(\omega) = \int_{-\infty}^{\infty} dt e^{i\omega t} \chi(t). \quad (11)$$

Here we will be primarily concerned with the loss induced by such an interaction, which is given by the imaginary component of Eq. 11

$$\chi''(\omega) \equiv \text{Im } \chi(\omega). \quad (12)$$

When the electromagnetic field interacts with the insulating sapphire samples, the loss described by Eq. 12 causes a decrease in the measured transmitted signal. However, when this drive is turned off and we enter the transient regime, the energy absorbed from the drive must now be re-emitted and ultimately measured from the output signal of the superconducting waveguide. To extract the radiated field, we perform homodyne detection, which involves extracting the classical output field quadratures  $I(t)$  and  $Q(t)$  and computing the amplitude  $A(t) = \sqrt{I^2(t) + Q^2(t)}$ . By input-output theory [46], the output field must be proportional to the dipole response,

$$A(t) \propto \langle \hat{P}(t) \rangle e^{i\omega_0 t}. \quad (13)$$

Thus, following Novotny *et. al.* [47], we can express the imaginary part of susceptibility,  $\chi''$ , using the experimentally obtained intensity  $\mathcal{I}(t) \propto A^2(t)$  as

$$\chi''(\omega) \propto \text{Im} \int_{-\infty}^{\infty} dt e^{i\omega t} \langle \mathcal{I}(t) \mathcal{I}(0) \rangle. \quad (14)$$

### C. Experimental Implementation

In principle, BCTDS can be performed on any dielectric sample at any temperature. Furthermore, even metallic or superconducting samples with oxide layers can be probed in reflection (Appendix D, Fig. 9). Here, we will be primarily interested in the dielectric response of TLS defects, which solely arise at cryogenic temperatures, as described in Sec. I. Therefore, to extract information about the TLS defects, we perform BCTDS on

our samples by inserting them into the waveguide and cooling them to 10 mK using a dilution refrigerator. As mentioned in the previous section, driven dielectric spectroscopy monitors the response during the pulse, while transient dielectric spectroscopy monitors the post-pulse region (also known as the ring-down).

To probe a driven dielectric response, we generate square pulses in the 3-5 GHz band, similar to those employed for superconducting-qubit gate operations. The simple square pulses we explore here are synthesized directly on an FPGA (Field Programmable Gate Array) board (AMD RFSoC 4x2) using the Quantum Instrumentation Control Kit (QICK) software package [48]. We send the pulses through a room-temperature amplifier (Minicircuits CMA-83LN+) and into a dilution refrigerator (Bluefors LD400) where they are attenuated and ultimately reach the 3D waveguide and interact with the sample (See setup diagram in Appendix F). The resultant signal is amplified using cryogenic high-electron-mobility transistor amplifiers from Low Noise Factory before being measured on the RFSoC.

Following the cessation of the external drive, the induced polarization in the medium relaxes, leading to a coherent emission in the transient dielectric response, which imprints the temporal decay of the ensembles of TLS defects on the outgoing field, allowing us to perform BCTDS. A strong time-dependent drive may also modify the phonon-induced decay rate of a TLS defect by hybridizing its states (dressed states), thereby shifting transition frequencies and enabling decay through induced sidebands. This may alter the coupling to the spectral density of the phonon bath, leading to either enhanced or suppressed relaxation depending on the drive strength. Although we do not investigate this effect here, the broadband nature of our technique should enable its detailed study in future experiments.

## III. RESULTS

### A. Cryogenic Dielectric Spectroscopy of Different Materials

As described in Sec. II A, our waveguide enables a modular characterization of the driven and transient dielectric response of ensembles of TLS defects in various samples. The samples considered in this study started with a 50.8 mm diameter, 432  $\mu\text{m}$  thick, wafer of ultra-high-purity HEMEX sapphire from Crystal Systems, which has been measured to have bulk loss tangents of the order  $10^{-8}$  using the dielectric dipper technique [13]. We spin coat the samples with photoresist and dice them into rectangular chips with  $27.5 \times 5.5$  mm dimensions. We clean the samples with solvents following a standard procedure described in Appendix B and mount them in the waveguide.

Figure 3 summarizes the dielectric spectroscopy results obtained for different materials. We perform room-

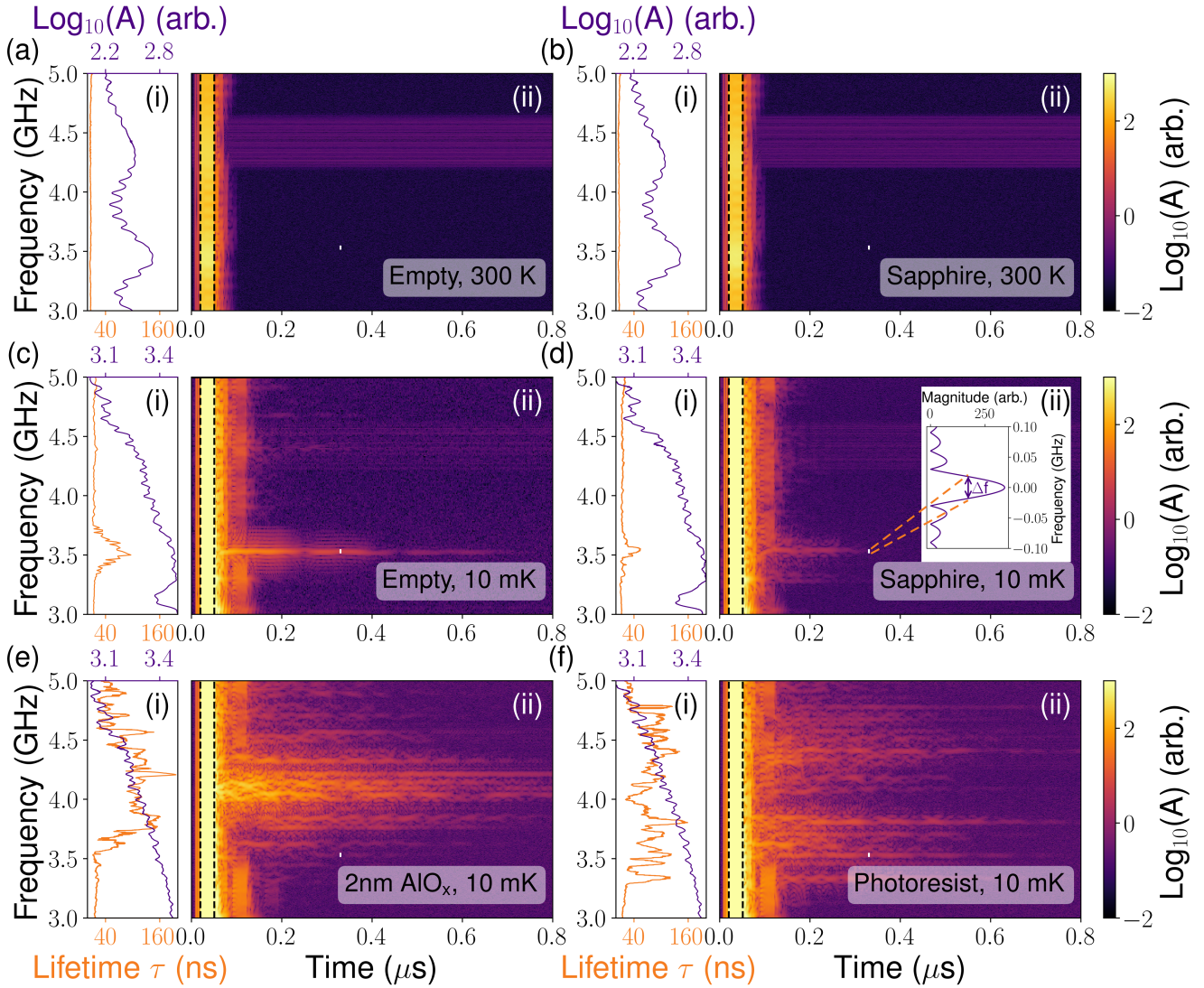


FIG. 3. Dielectric spectroscopy of different samples. We send a 30 ns pulse (marked by black dashed lines) and readout over a 0.8  $\mu$ s window (shown in subpanels (ii) with the color scale clipped to reveal weak transient features). Room temperature experiments for empty waveguide (a) and waveguide with solvent-cleaned sapphire samples (b) show no detectable response. The horizontal band around 4.4 GHz is due to electronic noise. Measurements (c)-(f) are performed at 10 mK, revealing coherent transient dielectric response features arising from TLS defects. Measurements (c) and (d) feature the same setups as (a) and (b), at 10 mK. (e) The same samples as (b) with a 2 nm aluminum oxide layer deposited via ALD. (f) The same samples as (b) with spin-coated Shipley 1813 photoresist. Transient response in (e)-(f) shows prominent features in the ring-down, which we attribute to increased TLS defect density. Subpanels (i) show the average driven dielectric response and the extracted lifetimes ( $\tau$ ) of the ring-downs, using an exponential fit. We include the FFT of the pulse in the inset in (dii) and mark the FWHM of the pulse,  $\Delta f$ , with a vertical white line, which has approximately the same bandwidth as the prominent spectral features.

temperature control experiments on an empty waveguide and on a waveguide with bare sapphire samples that serve as benchmarks, shown in Fig. 3(a) and 3(b), respectively. Given that the TLS defects observed in our experiments have frequencies between 3 and 5 GHz, small temperature changes can significantly impact their thermal occupation, a key signature that has been explored in previous work [49, 50]. Furthermore, increases in temperature cause thermal occupation of phonon modes, which can

lead to incoherent shaking of the double-well potential governing the TLS defects, likely broadening or destroying their spectral features. Our room temperature measurements in Fig. 3(aii) and 3(bii) confirm this thermal saturation effect.

As motivated in Sec. II C, when we cool down to cryogenic temperatures and remove this thermal effect, linear response theory suggests that the spectral dips of the driven dielectric response should be corroborated by

the longer-lived coherence times in the transient region. This is consistent with our findings when we cool down the same setups in Fig. 3(a) and 3(b) to 10 mK, we see an apparent narrowing of the spectral dips in the driven dielectric spectroscopy and a corresponding increase in the coherence of the transient dielectric response, shown in Fig. 3(c) and 3(d). These features are clear signatures of coherent energy storage and re-emission by the ensembles of TLS defects, which we discuss further in the context of master equation and Floquet theory in the next section (and with further investigations in Appendix G). In Fig. 3(c), we observe defect features in the absence of mounted samples, which we attribute to oxide layers present on the waveguide and antenna surfaces, and uncontrolled modes in the dilution fridge enclosure that couple to the waveguide. The signal in Fig. 3(d) likely originates from similar sources but may also include contributions from the solvent-cleaned sapphire samples in the waveguide, where residual surface contamination can result from leftover photoresist, adventitious carbon, or surface and dicing damages. In future work, we intend to remove these baseline contributions by retracting the samples *in situ* with a piezoelectric positioner, inspired by the dielectric dipper approach [13]. This calibration will enable further exploration of surface treatments such as etching, annealing, and passivation to reduce the measured transient dielectric response of bare sapphire and silicon wafers, which form the basis of all superconducting circuits [51–53].

Today, most Josephson junctions are fabricated using various versions of double-angle evaporation, where the insulating Josephson junction layer is formed from a native oxide grown on deposited aluminum. However, all regions of the chips that contain aluminum will inadvertently grow such native oxides, and therefore, most superconducting circuits inevitably contain large areas of aluminum oxide. To emulate the native oxide in Josephson junctions and on aluminum metal layers, we grow a thin, 2 nm aluminum oxide layer in an atomic layer deposition tool on a bare sapphire wafer. The results of these dielectric spectroscopy measurements are shown in Fig. 3(e). Here, we see clear signatures of ensembles of TLS defects, primarily in the transient region. The transient response exhibits pronounced collapse and revivals due to the interplay between external driving and TLS-defect ensemble interactions, clearly indicating memory effects [11, 54]. Furthermore, we want to highlight that the deposited 2 nm of aluminum oxide is approximately  $5 \times 10^{-6}$  times the volume of the substrate, but is composed of the same atomic species. These findings demonstrate the importance of material morphology in the existence and behavior of TLS defects and motivate future work on passivating metallic layers [55] and developing crystalline insulating layers for Josephson junctions. This work also suggests why tantalum, which hosts a thin, stoichiometric native oxide, is an advantageous material choice for high-coherence superconducting circuits [25, 51].

Finally, we also characterize the dielectric response of 1–4  $\mu\text{m}$  of photoresist on sapphire, as shown in Fig. 3(f). This investigation is especially relevant because most resonators and waveguides leverage photolithography, meaning residual photoresist may be left on substrates if improperly removed. These photoresists are complex polymer chains that likely contain a high density of TLS defects [56, 57] (a detailed description of sample preparation is included in Appendix B). By understanding the dielectric properties of the resist layer, we can better assess its impact on junction performance and guide fabrication and device design optimizations [43]. Therefore, in Fig. 3(f), we observe more transient response, consistent with our hypothesis that photoresist has many TLS defects.

The technique presented in this manuscript also enables future longitudinal studies where the sample can be characterized at each step of the fabrication process, and it envisions active mitigation strategies for these defects in the next generation of superconducting qubit devices. It is essential to highlight that in the data presented in Fig. 3, we observe that the transient emission processes have lifetimes on the order of 100 ns. Previous work on so-called dielectric echoes in JTWPAs experiments [40, 41] measured lifetimes of  $\approx 1 \mu\text{s}$ . Here, since the waveguide provides a large density of states and probes large ensembles, the lifetimes of these TLS defects may be reduced due to Purcell enhancement and stimulated emission. While the lifetimes extracted in these measurements are relatively short compared to state-of-the-art coherence times for superconducting qubits, the observed transient response can still play a prominent role in larger quantum circuits where gates are sequentially implemented. This effect may partially explain why large quantum circuits have overall fidelities lower than a naïve calculation based on single and two-qubit gate fidelities extracted using randomized benchmarking [58].

## B. Dielectric Response under Different Drive Lengths

In order to better examine the relationship between absorption in the driven dielectric response and the transient emission, we zoom into a narrower frequency range of 3.9–4.4 GHz and vary the pulse lengths in Fig. 4(a)–4(c), featuring 20 ns, 50 ns, and 200 ns pulses. Increasing the drive length improves the spectral resolution and reveals finer resonant features, which manifest themselves as sharper absorption dips during the pulse. After the drive is turned off, a similar effect is seen in the transient emission, where we observe sharper and more prolonged ringdowns. Without controlled access to the physical parameters of the TLS defects, it is encouraging to observe changes in the TLS dynamics as a result of different pulses. These findings support the feasibility of pulse-based coherent control of ensembles of TLS defects.

To explore the connection between spectral dips and

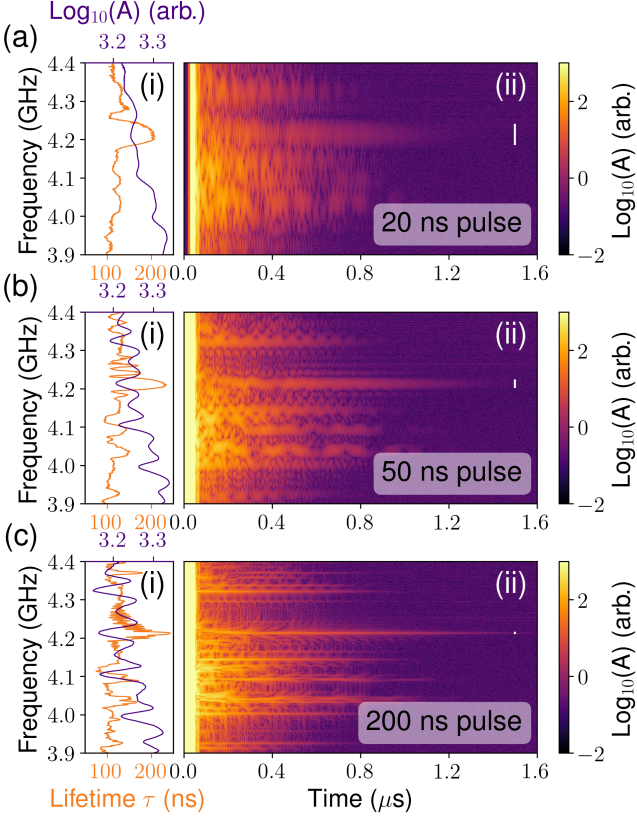


FIG. 4. Dielectric response of 2 nm aluminum oxide sample under different pulse lengths. (a) 20 ns pulse. (b) 50 ns pulse. (c) 200 ns pulse. Similar to Fig. 3, subpanels (ii) show the driven and transient dielectric response, while subpanels (i) show the average of the driven dielectric response and the extracted lifetimes ( $\tau$ ) of the transient dielectric response. As the pulse length increases, the bandwidth (marked by the short vertical white lines) of the pulse decreases, resulting in sharper emissions. Absorption in the pulsing region often corresponds to an emission around the same frequency, after the pulse is turned off.

the surrounding emission features, we performed numerical simulations of two interacting driven spins. The full pulse evolution was treated using a master equation, while the periodic portion of the drive was analyzed separately using Floquet formalism, as detailed in Appendix G and illustrated in Fig. 12. During the pulse, the system is dressed by the external periodic drive, resulting in the emergence of sidebands. The corresponding Floquet quasi-energies show clear dips in Fig. 12(b), and prolonged ring-downs within the vicinity of these dips, as seen in Fig. 12(a). In Fig. 13, we qualitatively reproduce the sharpening of ring-downs for different pulse durations as observed in the experiment.

### C. Further Investigation of Cryogenic Transient Dielectric Spectroscopy Results

In this section, we provide a more in-depth analysis of the transient dielectric response from the sample in Fig. 3(f) containing photoresist on sapphire, which is shown in Fig. 5. We start by plotting the transient dielectric response in Fig. 5(a(ii)) showing long-timescale oscillatory collapse and revival behavior of the emitted signal, which indicates information backflow and memory effects [59, 60]. This can be seen clearly in Fig. 5(a(i)), which displays the response at a single frequency of  $\omega/2\pi = 3.322$  GHz. To quantify the frequency components of the oscillations observed in the time traces in Fig. 5(a), we perform a FFT of all the data traces to generate Fig. 5(b(ii)). Again, a particular line cut at the same frequency is shown in Fig. 5(b(i)). The FFT shows clear V-shaped features and horizontal bands, particularly in the 3.65–4.0 GHz and 4.25–4.65 GHz ranges. These V-shapes arise from off-resonant emission by dominant eigenfrequencies of the ensembles of TLS defects, made visible by the broadband response of the waveguide [61]. Numerical simulations of a driven, interacting four-spin system (Appendix G, Fig. 13) confirm this behavior, namely the appearance of V-shaped arcs in the FFT, which sharpen with longer pulse durations, and converge toward the bare eigenmode frequencies.

We also compute the two-time correlation function  $g^2(\tau')$  [62]

$$g^{(2)}(\tau') = \frac{\langle \mathcal{I}(t)\mathcal{I}(t+\tau') \rangle}{\langle \mathcal{I}(t) \rangle^2}, \quad (15)$$

where  $\mathcal{I}(t) \propto A^2(t)$  is the intensity of the transmitted pulse, and plot it in Fig. 5(c).  $g^{(2)}(\tau')$  provides us with a map of temporal correlations and displays evident non-exponential, oscillatory decay, which is a hallmark signature of memory effects or non-Markovian dynamics of the ensembles of TLS defects. Finally, we utilize the computed  $g^{(2)}(\tau')$  to extract  $\chi''(\omega)$  using Eq. 14, which we show in Fig. 5(d). Here, consistent with  $g^{(2)}(\tau')$ , we observe non-monotonic and negative  $\chi''(\omega)$ , highlighted by the cyan contours at zero in Fig. 5(d), exhibiting partial overlap with the aforementioned V-shapes in some regions of the FFT. This behavior indicates physics beyond linear response and further supports the presence of memory effects and re-emission in the ensembles of TLS defects [63, 64].

## IV. CONCLUSIONS AND OUTLOOK

This work introduces BCTDS, a technique to probe TLS defects that supports fast and modular mounting of various samples, without invoking narrow-band probes like resonators or qubits. Our measured cryogenic dielectric spectroscopy experiments reveal distinct transient features and memory effects as demonstrated by

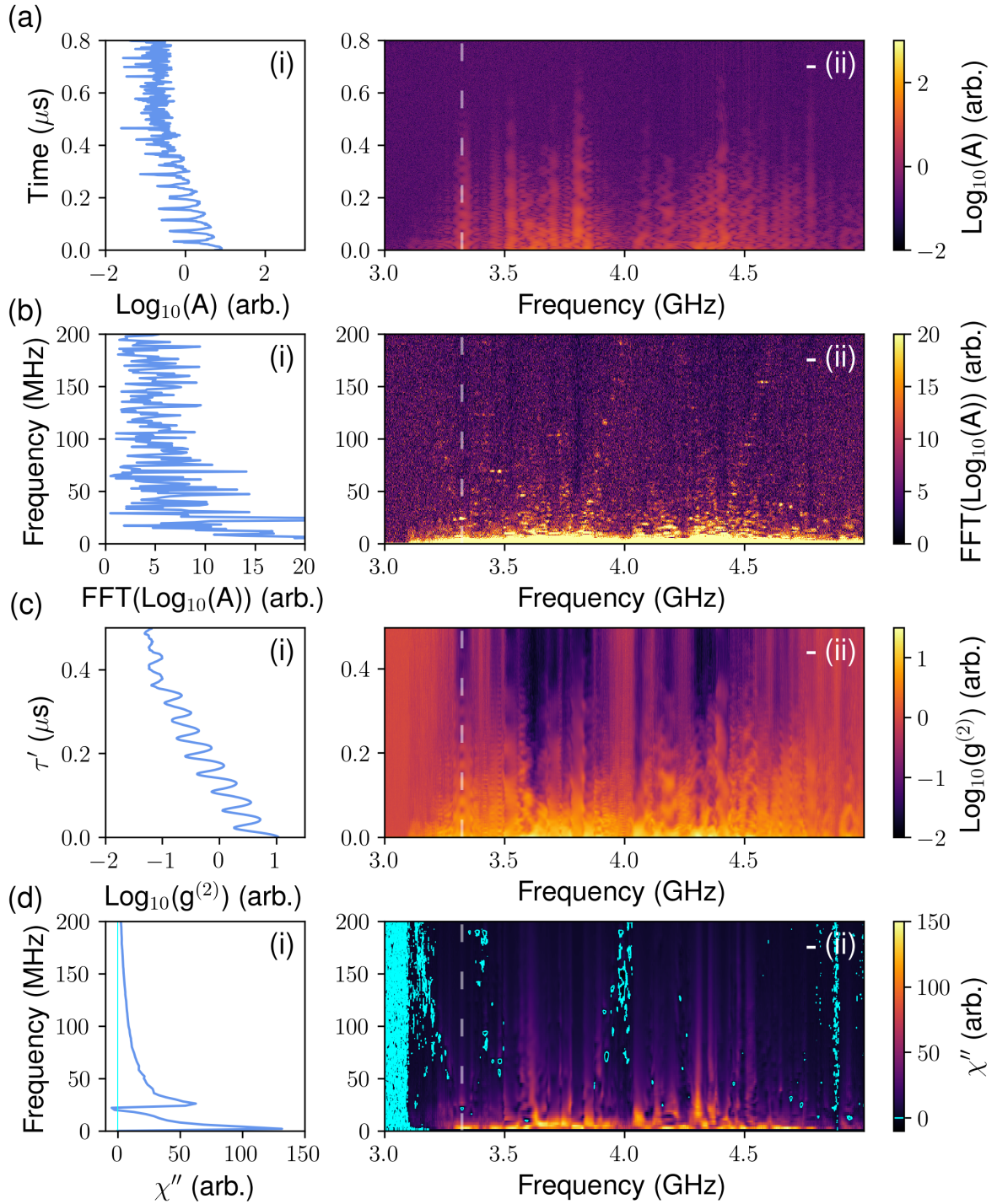


FIG. 5. Transient dielectric response of Shipley 1813 photoresist on sapphire. We use the same data as Fig. 3(f). (aii) Logarithmic magnitude of the transient dielectric response. (bii) Magnitude of Fast Fourier transform (FFT) of the logarithmic amplitude. (cii) Log of the two-time correlation function  $g^{(2)}$  map of the transient spectrum, defined by Eq. 15. (dii)  $\chi''$  computed from  $g^{(2)}$  using Eq. 14. We highlight transitions from positive to negative  $\chi''$  with the cyan contour in (dii). Subpanels (i) show linecuts at  $\omega/2\pi = 3.322$  GHz, marked by dashed line in (ii), highlighting distinct memory effects in the form of collapse and revivals in the ringdown (a), sharp spectral features in the FFT (b), non-exponential decay, bunching, and oscillations indicative of non-Markovian dynamics (c), and non-monotonic and negative  $\chi''$  (d). The negative regions are consistent with the bright FFT features in (bii). It should be noted that  $\chi''$  oscillates around zero near  $\omega/2\pi = 3$  GHz primarily due to weak signals and not necessarily indicating memory effects. A short horizontal white line is added to indicate pulse bandwidth  $\Delta f$ .

the  $g^{(2)}$  and  $\chi''$  plots in Fig. 5(c), 5(d), respectively. Such memory effects may indicate that the dynamics are non-Markovian, which may be detrimental for quantum error correction if manifested in quantum processors [54, 65, 66]. We believe that much of the memory effects arises from the interplay between coherent TLS defect interactions and driving and measuring in a broadband environment. By analyzing the frequency and temporal correlations of large ensembles of TLS defects in isolated materials, we take initial steps toward uncovering the atomistic structure of TLS defects. Next, we aim to introduce an orthogonal SMA port to rotate the polarization of the drive and perform the same dielectric spectroscopy experiments, subject to different drive strengths. By integrating over different drive polarizations, we can better understand the frequency distribution and dipole moments of the TLS defects in various samples.

While this work has focused on materials for superconducting qubits, we highlight that BCTDS is a more general technique that provides information about the loss of various dielectric materials. This study is also not exclusively applicable to TLS defects; for instance, we can use BCTDS to measure vacancies and boron dopants in silicon and nitrogen vacancies in diamond directly, without the need for optical interrogation [67]. In conclusion, we have demonstrated a novel spectroscopy tool based on a broadband 3D waveguide that enables global interrogation of ensembles of TLS defects. The approach is entirely modular, and we demonstrate that this can be leveraged for longitudinal devices that can help develop causal relationships between properties of ensembles of TLS defects and material processing steps.

## DATA AVAILABILITY STATEMENT

The data that support the findings of this study are available from the corresponding author upon reasonable request.

## ACKNOWLEDGMENTS

Bert Harrop graciously diced the devices at Princeton. Sofia Abrego and Chloe Buschmann helped review and polish the manuscript. We also acknowledge stimulating conversations with Kater Murch, Miles Blencowe, Geoffroy Hautier, Chandrasekhar Ramanathan, and Valla Fatemi. Startup funds from the Thayer School of Engineering at Dartmouth primarily supported this work. While the scientific focus of this work is quite distinct from existing funding, M.F. would like to express gratitude for the support of science within his group through the DARPA Young Faculty Award No. D23AP00192 and NSF PHY-2412555, and hopes that projects like this continue to be made possible by grants from the US federal government. The views and conclusions in this manuscript are those of the authors. They should not be

interpreted as representing the official policies, expressed or implied, of DARPA, the NSF, or the US Government. The US Government is authorized to reproduce and distribute reprints for Government purposes, notwithstanding any copyright notation herein.

## AUTHOR CONTRIBUTIONS

M.F. proposed the waveguide approach and guided the experimental and theoretical work. Q.W. performed the experiments, made the figures, and developed the data analysis pipeline for this work. S.M.G. and J.F. designed and fabricated the waveguide. J.S.S.G., R.L., and S.B. provided theoretical support. J.S.S.G., S.B., and M.F. provided context for the work. S.B. provided theoretical insights using an interacting-driven TLS model to validate the observed patterns. All authors jointly validated the results and participated in the writing of the manuscript.

## COMPETING INTERESTS

The authors declare no competing interests.

## ADDITIONAL INFORMATION

### Correspondence and request for materials

Correspondence and material requests should be directed to Mattias Fitzpatrick (mattias.w.fitzpatrick@dartmouth.edu). Data supporting the findings of this study are available from the corresponding author upon reasonable request.

## Appendix A: Waveguide Design and Fabrication

### 1. Waveguide Design

The fundamental building block of our waveguides is an adapter that provides a  $50\ \Omega$  impedance-matched conversion between an SMA coaxial cable and a WR-229 3D rectangular waveguide. To understand the basic features of the waveguide, we solve the wave equation for a rectangular prism, with boundary conditions that the electric field goes to zero at the walls of the waveguide. After performing separation of variables, we can identify a set of allowed eigenmodes for the cross section perpendicular to the direction of propagation, with wavenumbers given by

$$k_c = \sqrt{\left(\frac{m\pi}{a}\right)^2 + \left(\frac{n\pi}{b}\right)^2}, \quad (A1)$$

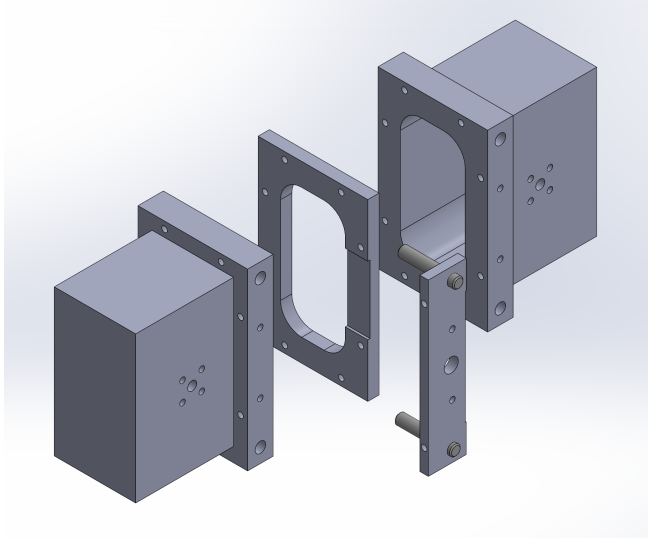


FIG. 6. Exploded view of waveguide assembly.

where  $a$  and  $b$  are the width and height of the rectangular cross-section of the waveguide, respectively. The constants  $m$  and  $n$  are integers whose combinations identify different eigenmodes of the cross-section. This means that the propagation constant of the transmitted wave can be expressed as

$$\beta = \sqrt{k^2 - k_c^2}, \quad (\text{A2})$$

where  $k$  is the wavenumber. Significantly, Eq. A2 predicts that when  $k^2 < k_c^2$ ,  $\beta$  becomes imaginary, and the solutions become decaying exponentials along the waveguide in a domain known as the waveguide's cutoff [14]. Therefore, we can describe the frequencies of the allowed modes of the waveguide using

$$f_{c_{mn}} = \frac{k_c c}{2\pi}, \quad (\text{A3})$$

where  $c$  is the speed of light. From Eq. A3, we then identify the cutoff frequency, which is the lowest frequency  $\text{TE}_{10}$  mode, given by

$$f_{c_{10}} = \frac{c}{2a}, \quad (A4)$$

assuming that  $a \geq b$ . The cutoff frequency formula provided in Eq. A4 is idealized and assumes a perfect rectangular waveguide, which is challenging to manufacture in practice due to the sharp inner corners. Therefore, we utilize Ansys HFSS to consider the design of the actual waveguide in this work. The drive and readout ports are coaxial SMA cables that transition into small antennas integrated into the waveguide. This coupling scheme smoothly transforms the coaxial mode of the SMA cables to a close approximation the  $TE_{10}$  mode of an ideal rectangular waveguide, producing a polarized electric field that will ultimately couple to the TLS defects in the sample.

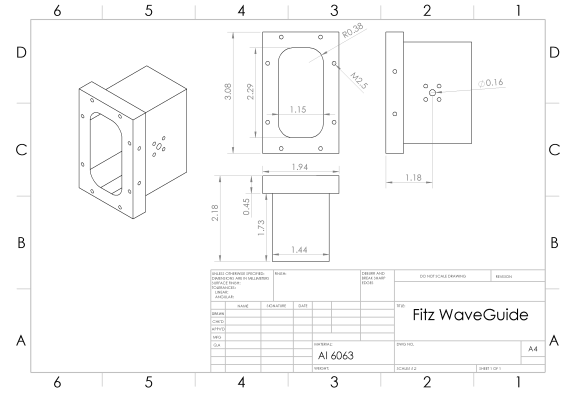


FIG. 7. Designs for SMA to WR-229 3D rectangular waveguide adapter utilized to build the 3D waveguide.

Figure 7 provides detailed dimensions of our SMA to WR-229 3D rectangular waveguide adapter. In this work, we leverage Eq. A4 to achieve the desired 3 to 6 GHz frequency band and adapt the perfect rectangular waveguide designs to make the manufacturing easier. In particular, our design features an inner radius of the 3D waveguide designed to use a 3/8 inch end mill. M2.5 screws are used to mount the 4.1 mm SMA pins that integrate into the designs shown in Fig. 7.

We fabricate two copies of the SMA to WR-229 3D rectangular waveguide adapter to construct a full waveguide. Then, we construct a clamp for samples that can be introduced between the two waveguide adapters. This approach allows us to consider a variety of sample layouts and sizes. The assembly of the complete waveguide can be seen in Fig. 6.

## 2. Waveguide Fabrication

The waveguide used in this manuscript is manufactured from Aluminum 6061 using a HAAS Super Mini Mill in Dartmouth's Thayer School of Engineering machine shop. A combination of steel wire wool and polishing stones was used to improve the surface finish, especially the rounded corners, and remove any feed marks left behind from the end mill. Finally, the waveguide was cleaned using isopropanol (IPA) to remove impurities and oily residues.

## Appendix B: Sample Processing

To demonstrate the modularity of our platform, we consider three types of samples, the preparation of which is explained in this section.

We start with high-grade crystalline 0.5 mm-thick sapphire wafers from Crystal Systems, which are then diced into 27.5 x 5.5 mm rectangular strips, the standard substrate size for hosting 3D transmons. The samples are

initially covered in resist AZ 1518 to protect them from debris during dicing (likely another source of TLS defects). We soak the chips in acetone at 70 °C overnight and sonicate them in acetone before transferring them to IPA and drying with compressed nitrogen gas.

To study the effects of photoresist on the TLS density, we spin-coat Shipley 1813 with thicknesses ranging from 1 to 4  $\mu\text{m}$ . We also study the oxide layers (typically a few nanometers in thickness), another candidate source of TLS defects. Instead of evaporated aluminum, which would give both an aluminum and oxide layer, we used an atomic layer deposition (ALD) machine to grow a 2 nm thin film. We expect the entire film to be oxidized by doing 20 burst cycles at 80 °C and repeatedly using  $\text{H}_2\text{O}$  as an oxidant at each burst.

### Appendix C: Cryogenic Dielectric Spectroscopy of the Same Sample, For Different Cooldowns

Two-level system (TLS) defects are known to shift in frequency and spatial location after thermal cycling [68], due to rearrangements in the disordered environment that reshape the local energy landscape. To corroborate this signature, we perform dielectric spectroscopy experiments 15 days apart on the same sample subject to a thermal cycle to 300 K in Fig. 8. As expected, we see a significantly different driven and transient dielectric response in Fig. 8(a) and 8(b), highlighted by the difference plot in Fig. 8(c). In future work, we intend to perform systematic studies of the temperature dependence closer to 10 mK. Such studies may provide insight into the observed ‘universal dielectric response’, and potentially probe the transition of quantum TLS defects to the broad classical dielectric response [69, 70].

### Appendix D: Dielectric Response in Transmission and Reflection

For ideal, lossless systems, transmission and reflection contain equivalent information as incident power must be conserved. In our experiment, where dissipation is present, reflection provides complementary information about dielectric loss during the pulsing region. We make measurements on the same samples as in Appendix C but place a cryogenic circulator at the waveguide input to measure both the transmission (Fig. 9(a)) and reflection (Fig. 9(b)) signals. In the transient region, emission from the dielectric samples is detected almost equally in the transmission and reflection channels, as the samples are positioned equidistant from the two antenna pins, and the readout circuits are identical. As a result, the collected signal shows minimal difference, as shown in Fig. 9(c). A short vertical white line is added to indicate pulse bandwidth  $\Delta f$ .

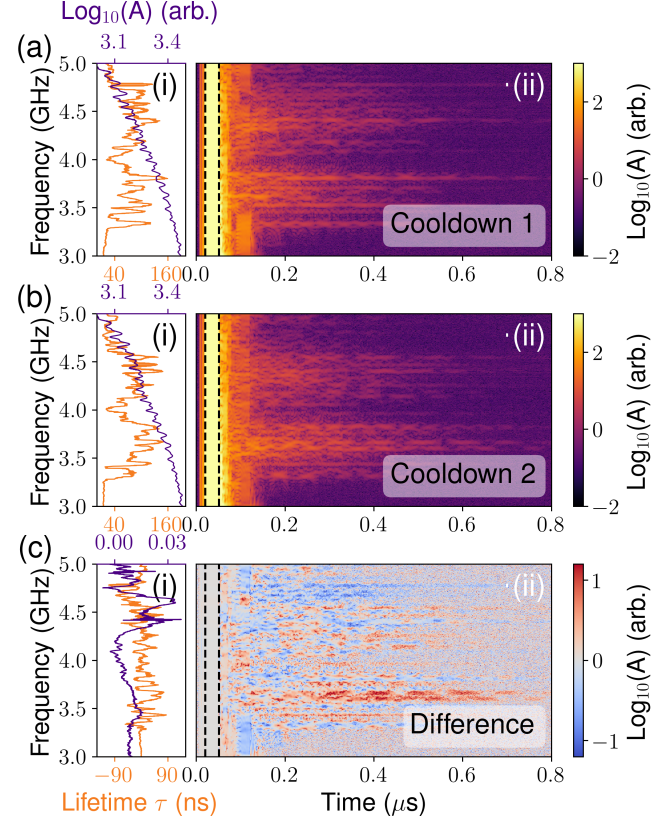


FIG. 8. Cryogenic dielectric spectroscopy measurements of Shipley 1813 photoresist on sapphire over different cooldowns. (a) Cooldown 1, using the same data as Fig. 3(f). (b) Cooldown 2, with the same sample as (a), but after warming up to 300 K. (c) Difference in dielectric response between cooldowns 1 and 2, demonstrating completely distinct spectral fingerprints. Note that the datasets in (a) and (b) were acquired 15 days apart, meaning that some of the change in the dielectric response could be due to subtle drifts of the TLS defects at cryogenic temperatures, which are known to happen. However, the predominant changes are likely morphological, primarily from thermal cycling. A short vertical white line is added to indicate pulse bandwidth  $\Delta f$ , similar to Fig. 3(d).

### Appendix E: Electric Field Amplitude Calibration

The waveguide design ensures that the transmitted signal is relatively constant over a bandwidth of approximately 3-6 GHz, shown in Fig. 2(b). However, the samples under test are coupled in the middle of the waveguide, which can be frequency-dependent, as illustrated in Fig. 10(a). We leverage HFSS simulations to predict the average electric field amplitude at the sample plane over our frequency bandwidth  $\Delta f$ , plotted in blue dots and lines in Fig. 10(b). To compensate for this variation, we apply a frequency-dependent scaling factor (red solid line). The impact of this calibration is evident when comparing the transient spectra of a sapphire sample with an AlOx deposit before (Fig. 10(c)) and after (Fig. 10(d)) apply-

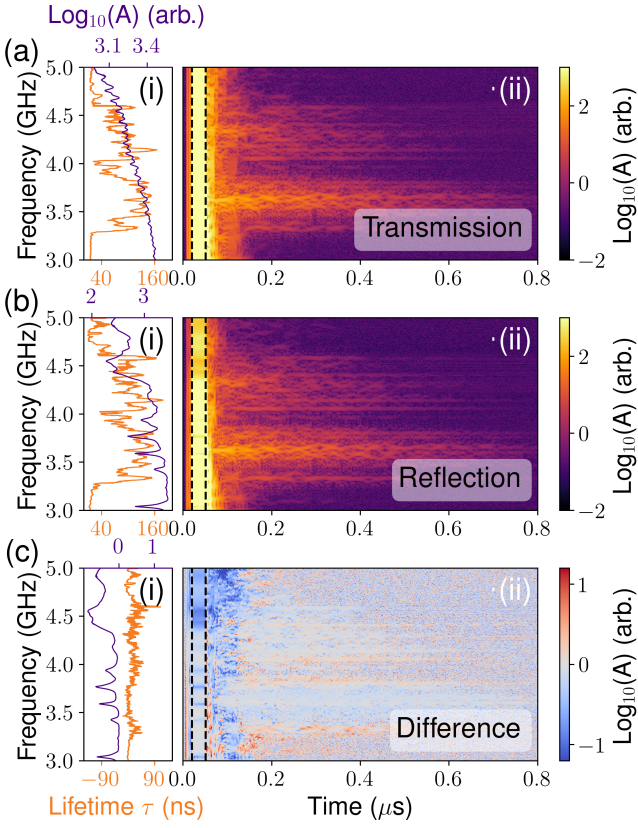


FIG. 9. Dielectric response of Shipley 1813 photoresist on sapphire measured in transmission and reflection. We used the same samples as in the thermal-cycling experiment in Fig. 8, but we add a cryogenic circulator (QCY-G0400801) to the waveguide input to measure both the transmitted (a) and reflected (b) signals. We also include a difference plot (c), which shows a similarity in response from the transient region.

ing the correction. Significantly, most of the key features in the data remain. Still, such calibrations can ensure uniform electric field densities as a function of frequency and may prove critical in future experiments to deduce properties of individual ensembles of TLS defects.

#### Appendix F: Measurement Setup

This work utilizes an AMD radio-frequency system on a chip (RFSoC) board, which provides a fast sampling rate (9.85 GSPS for DAC and 5 GSPS for ADC) and direct synthesis and readout of microwave pulses without needing up- and down-conversion. To control the RFSoC, we utilize the Quantum Instrumentation Control Kit, a Python package developed by Fermi National Accelerator Laboratory [71].

The pulses generated from the RFSoC pass through a room-temperature amplifier (Minicircuits CMA-83LN+) and a series of attenuators at various temperature stages

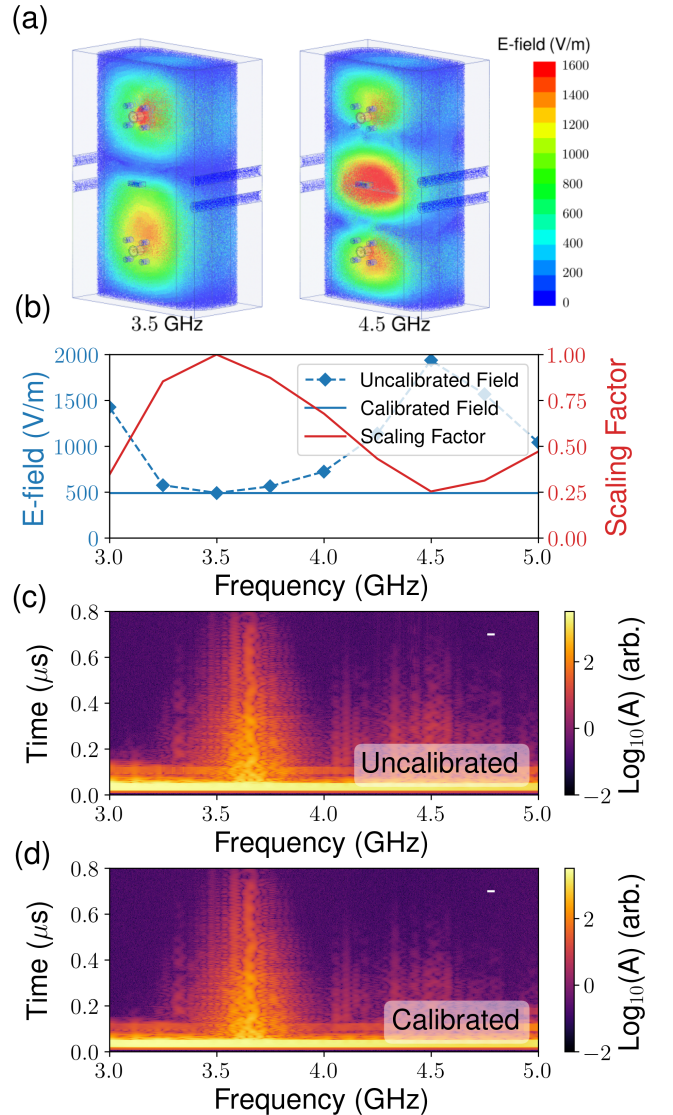


FIG. 10. Electric field amplitude calibration at the sample plane. (a) HFSS simulation of the electric field distribution in the waveguide at 3 GHz and 5 GHz. The simulation applies an input power of 1 W at the SMA port to excite the dominant mode. The snapshot is taken for both frequencies when the oscillating electric field reaches its maximum amplitude at the sample plane. (b) Frequency-dependent electric field strength averaged over the sample plane and time (blue solid line). A scaling factor is applied to the pulse (red solid line) to achieve a uniform drive amplitude across the band, reducing the amplitude in regions with higher intrinsic field strength. The resulting average field profile is flattened (blue dashed line). (c)-(d) Comparison of transient spectra for a sapphire sample with AlOx deposit (same sample as Fig. 3(e) with a change in mounting configuration). We show the spectrum before (c) and after (d) field calibration. The calibrated spectrum shows reduced amplitude in previously over-driven regions and yields a more uniform interrogation of the ensembles of TLS defects across the full spectral range. A short horizontal white line is added to indicate pulse bandwidth  $\Delta f$ .

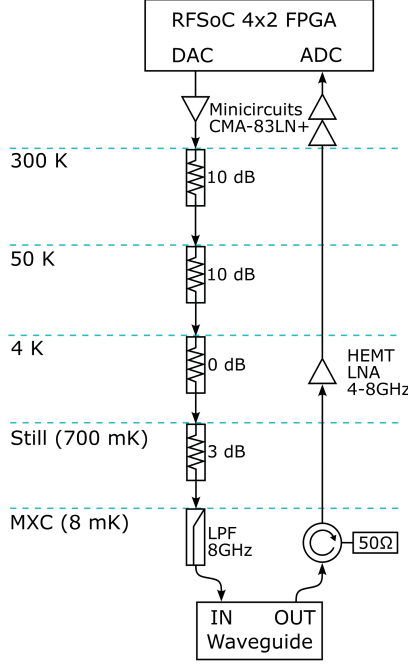


FIG. 11. Measurement setup for transient dielectric spectroscopy.

of a Bluefors LD400 dilution refrigerator. The signal reaches the waveguide input port at base temperature (typically  $< 10$  mK) and interacts with the sample (Fig. 11). The output signal from the waveguide is collected using a readout SMA pin that then passes through a cryogenic circulator, HEMT (High Electron Mobility Transistor) amplifier, and two room-temperature amplifiers (Minicircuits CMA-83LN+), before returning to the RFSoC. A detailed wiring diagram is provided in Fig. 11.

#### Appendix G: Qualitative Comparison to Numerical Simulations

The purpose of the numerics is to qualitatively reproduce the key experimental observation that the Fourier spectra exhibit broad sidebands for short pulses, which progressively sharpen as shown in Fig. 4 in the main text. To this end, we model the system using a driven-spin model with a finite-duration pulse, which provides a simplified framework for interpreting the interference patterns observed in the TLS ring-down and understanding how the applied drive shapes the dynamics. During this interval, the system is expected to exhibit Floquet-like physics, with the dynamics governed by the quasienergy spectrum and associated sidebands. After the end of the pulse, signatures of the prior Floquet dynamics may persist in the post-pulse evolution, manifesting as coherent oscillations or ringdown features. To support this interpretation, we briefly summarize the Floquet formalism and illustrate the emergence of sidebands using numeri-

cal simulations. We first briefly summarize the formalism following [72, 73]. Consider a time-periodic Hamiltonian  $H(t)$  with period  $T$ ,

$$H(t+T) = H(t), \quad (G1)$$

and define the Floquet frequency  $\Omega = \frac{2\pi}{T}$ .

Floquet theorem states that solutions to the time-dependent Schrödinger equation are as follows.

$$i \frac{d}{dt} |\psi(t)\rangle = H(t) |\psi(t)\rangle \quad (G2)$$

can be expressed as

$$|\psi_\alpha(t)\rangle = e^{-iE_\alpha t} |u_\alpha(t)\rangle, \quad (G3)$$

where the Floquet mode  $|u_\alpha(t)\rangle$  is periodic,

$$|u_\alpha(t+T)\rangle = |u_\alpha(t)\rangle, \quad (G4)$$

and  $E_\alpha$  is the quasi-energy of Floquet.

Expand  $|u_\alpha(t)\rangle$  into Fourier harmonics,

$$|u_\alpha(t)\rangle = \sum_{m=-\infty}^{\infty} e^{-im\Omega t} |u_\alpha^m\rangle, \quad (G5)$$

leading to the eigenvalue equation in the extended space

$$\sum_m \mathcal{H}_{nm} |u_\alpha^m\rangle = E_\alpha |u_\alpha^n\rangle, \quad (G6)$$

where

$$\mathcal{H}_{nm} = H_{n-m} + m\Omega \delta_{nm}, \quad H_k = \frac{1}{T} \int_0^T dt e^{ik\Omega t} H(t). \quad (G7)$$

For a monochromatic drive

$$H(t) = H_0 + V e^{i\Omega t} + V^\dagger e^{-i\Omega t}, \quad (G8)$$

the Floquet Hamiltonian  $\mathcal{H}$  is block-tridiagonal:

$$\mathcal{H} = \begin{pmatrix} \cdots & \vdots & \vdots & \vdots & \cdots \\ \cdots & H_0 - \Omega & V & 0 & \cdots \\ \cdots & V^\dagger & H_0 & V & \cdots \\ \cdots & 0 & V^\dagger & H_0 + \Omega & \cdots \\ \cdots & \vdots & \vdots & \vdots & \ddots \end{pmatrix}. \quad (G9)$$

The dipole operator  $\hat{P}(t)$  defines the polarization. The dipole response function is given by the retarded commutator.

$$\chi(t, t') = -i\theta(t - t') \langle [\hat{P}(t), \hat{P}(t')] \rangle, \quad (G10)$$

where  $\theta$  is the Heaviside step function and  $\langle \cdot \rangle$  is the expectation in the steady-state Floquet. Using Floquet states, the response can be expanded as

$$\chi(t, t') = \sum_{n,m} e^{-in\Omega t} e^{im\Omega t'} \chi_{nm}(t - t'), \quad (G11)$$

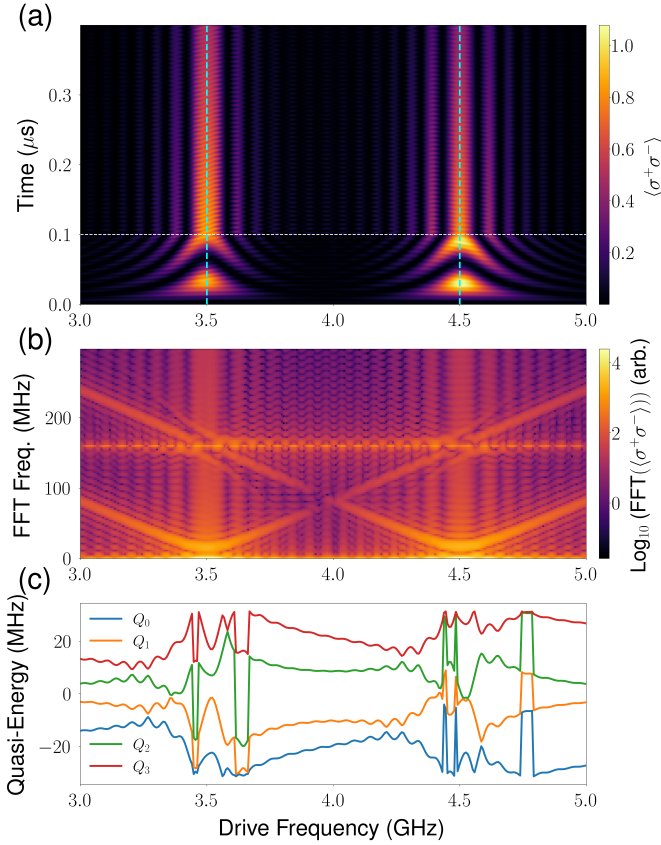


FIG. 12. Numerical simulation of collective excitation dynamics and Floquet quasi-energies in a driven two-spin system ( $N = 2$ ). (a) Time-domain evolution of the collective population  $\langle \sigma^+ \sigma^- \rangle$  obtained by solving the Lindblad master equation for a square cosine pulse with dipole-dipole coupling  $J = 50$  MHz, drive amplitude  $A = 100$  MHz, pulse duration  $\tau = 100$  ns (horizontal dashed line), collective dissipation rate  $\Gamma = 2.0$  MHz, and bare transition frequencies  $\epsilon_1 = 3.5$  GHz and  $\epsilon_2 = 4.5$  GHz (vertical dashed lines). (b) Amplitude of the corresponding Fourier spectra of the time-domain response for the entire evolution as a function of drive frequency, revealing pronounced V-shaped spectral features that converge towards the bare TLS frequencies. (c) Floquet quasi-energies (first four) computed during the driving period. Pronounced features appear near the driving frequencies that lead to long-lived ring-downs observed after the pulse is off in (a).

where the Fourier components satisfy the Dyson equation

$$\chi_{nm}(\omega) = \chi_{nm}^0(\omega) + \sum_k \chi_{nk}^0(\omega) V_{km} \chi_{km}(\omega). \quad (G12)$$

Explicitly, the Fourier transform of the dipole response function is expressed via the Floquet Green's functions, as

$$\chi_{nm}(\omega) = \sum_{\alpha, \beta} \sum_l \frac{d_{\alpha\beta}^l d_{\beta\alpha}^{m-n-l}}{\omega - (E_{\alpha} - E_{\beta} + l\Omega) + i\eta}, \quad (G13)$$

where  $d_{\alpha\beta}^m = \frac{1}{T} \int_0^T dt e^{im\Omega t} \langle u_{\alpha}(t) | \hat{P} | u_{\beta}(t) \rangle$  are the elements of the Floquet dipole matrix,  $\eta \rightarrow 0^+$ , and the poles

$$\omega = E_{\alpha} - E_{\beta} + l\Omega \quad (G14)$$

determine the resonance frequencies.

When the system is driven by a periodic square pulse of duration  $\tau$ , then turned off at  $t = \tau$ , the system freely evolves with no drive for  $t > \tau$ . The post-pulse time evolution contains oscillatory terms at frequencies set by quasi-energy differences  $E_{\alpha} - E_{\beta}$  and sideband shifts  $l\Omega$ , weighted by the residues of these poles in  $\chi$ . These produce ring-down oscillations, whose decay rates reflect the imaginary parts of  $E_{\alpha}$ .

For a driven two-level system with detuning  $\epsilon$  and external field amplitude  $A$ , the time-dependent Hamiltonian is given by

$$H(t) = \frac{\epsilon}{2} \sigma_z + A \cos(\Omega t) \sigma_x, \quad (G15)$$

Here, the periodic drive induces dressed states with quasi-energies

$$E_{\pm, m} \approx \pm \frac{\epsilon}{2} + m\Omega, \quad (G16)$$

which hybridize near multi-photon resonances  $\epsilon \approx n\Omega$ .

The effective coupling strength of  $n$  photons is proportional to  $2AJ_n(\frac{2A}{\Omega})$  where  $J_n$  is a Bessel function of the first kind. This effective coupling changes the size of the avoided crossing near multi-photon resonance. These avoided crossings form characteristic V-shaped structures near resonances in the  $(\epsilon, \Omega)$  plane, where the arms of the V correspond to bare energy levels shifted by multiples of  $\Omega$ , and the vertex marks the opening of a gap due to multi-photon coupling. The tree-like structures observed in the ringdowns arise from the interference of multiple sideband emissions. Unlike the case of a single driven two-level system, our system consists of an ensemble of interacting TLSs coupled via dipole-dipole interactions. As a result, each eigenstate of the bare, time-independent Hamiltonian becomes dressed by the external drive, leading to more complex interference effects that manifest as beatings in the observed signal.

Although the discussion above focuses on a single two-level system for illustrative purposes, our numerical simulations consider systems with  $N = 2$  and  $N = 4$  coupled spins, incorporating weak dipole-dipole interactions, which are three orders of magnitude smaller than the individual TLS frequencies. Using this model, we observe collapse and revival patterns that qualitatively resemble the experimental observations. The Fourier transform of the simulated dynamics reveals characteristic V-shaped features in the spectral domain, converging at the bare eigenfrequencies of the coupled system. Dissipation is modeled through a collective radiative decay channel using the Lindblad master equation, which may

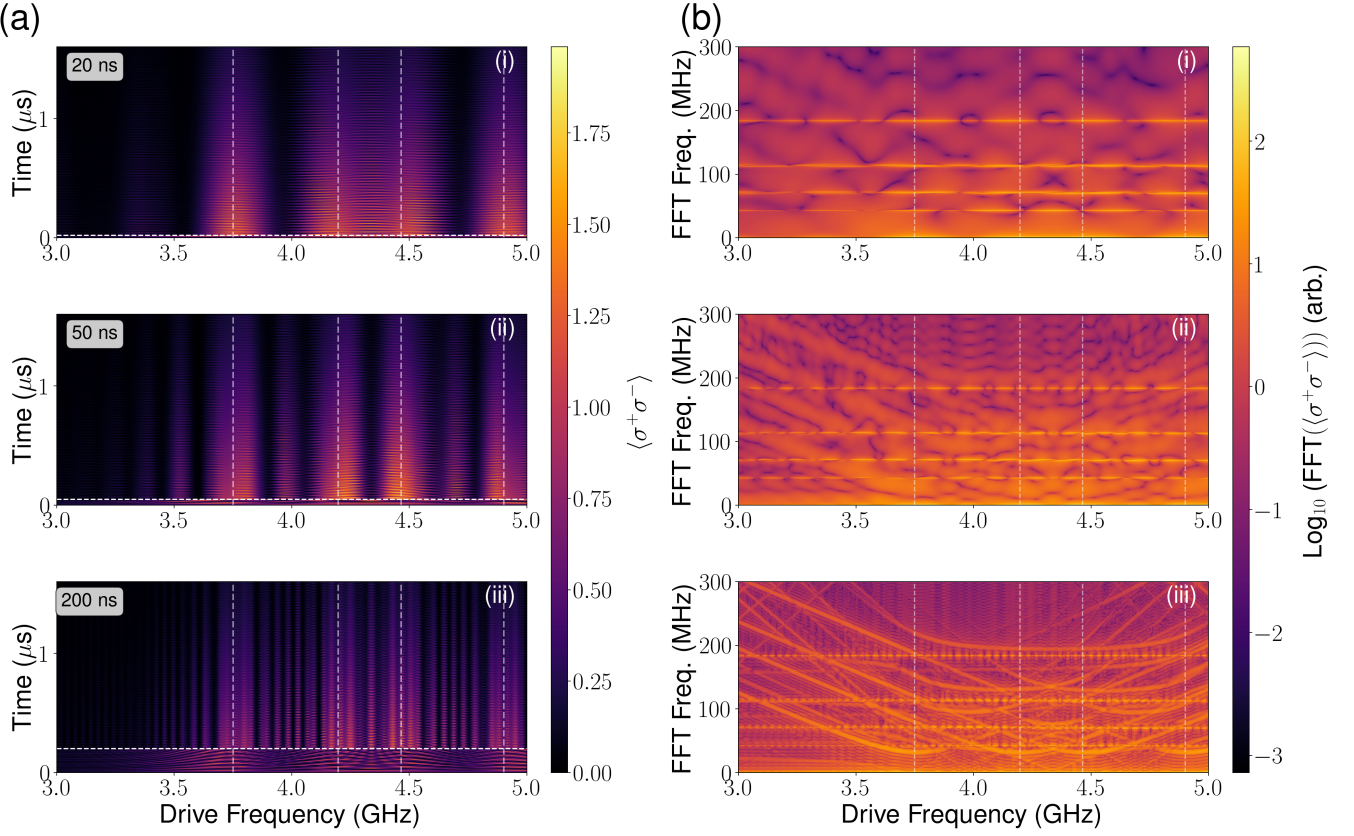


FIG. 13. Numerical simulation of a driven, interacting four-spin system ( $N = 4$ ) using the Lindblad master equation. The plots show a single disorder realization of an all-to-all connected spin network with randomly assigned bare frequencies and dipole-dipole couplings, drawn from uniform distributions  $\epsilon \in [3.0, 5.0]$  GHz and  $J \in [-50.0, 50.0]$  MHz, respectively. The system is subject to a collective radiative decay rate  $\Gamma = 1.0$  MHz and a drive amplitude  $A = 400$  MHz. (a) Time evolution of the collective TLS population  $\langle \sigma^+ \sigma^- \rangle$  as a function of drive frequency for pulse durations  $\tau = 20$  (i), 50 (ii), and 200 (iii) ns. Tree-like ring-down structures emerge, becoming increasingly sharp with longer pulses. (b) Corresponding Fourier spectra reveal broad sidebands for short pulses that progressively sharpen and converge toward the system's bare eigenfrequencies as  $\tau$  increases, giving rise to a distinct V-shaped pattern. The bare TLS frequencies are indicated by vertical dashed lines in (a) and (b), while the pulse duration is marked by a horizontal white dashed line in (a).

be justified in our setup due to the presence of a broadband waveguide mediating the system–environment interaction. Hence, including interactions and collective dissipation, the Hamiltonian becomes [19]

$$\hat{H}(t) = \sum_{j=1}^N \hat{H}_{0,j} - \hat{\mathbf{P}} \cdot \mathbf{E}(t) + \sum_{i < j} J_{ij} \hat{\sigma}_x^{(i)} \hat{\sigma}_x^{(j)}. \quad (\text{G17})$$

The dynamics is governed by the Lindblad master equation.

$$\frac{d\rho}{dt} = -i [\hat{H}(t), \rho] + \Gamma (2\hat{S}_- \rho \hat{S}_+ - \hat{S}_+ \hat{S}_- \rho - \rho \hat{S}_+ \hat{S}_-), \quad (\text{G18})$$

where  $\hat{S}_\pm = \sum_{j=1}^N \hat{\sigma}_\pm^{(j)}$  are collective lowering and raising operators. The assumption of collective decay is motivated by the broadband nature of the waveguide, which couples similarly to all TLSs.

Figure 12 shows numerical simulations of the collective

excitation dynamics and Floquet quasi-energies in a two-spin system. Panel (a) displays the time evolution of the collective population, obtained by solving the Lindblad master equation with fixed dipole-dipole coupling, drive amplitude, pulse duration (marked by a horizontal dashed line), collective dissipation, and two distinct TLS frequencies (indicated by vertical dashed lines). During the drive, clear Rabi-Chevron patterns emerge, while following the pulse, pronounced interference and long-lived ring-down oscillations are observed. Figure 12(b) shows the Fourier amplitude of the full time-domain simulation as a function of drive frequency. The V-shaped features converging toward the bare TLS frequencies reflect detunings between the drive and the individual transitions. These structures highlight the coherent excitation conditions that give rise to the long-lived ring-downs observed in panel (a). Figure 12(c) displays the first four Floquet quasi-energies computed during the driving period. The quasi-energy spectrum exhibits characteristic dips near

the driving frequencies, which correspond to resonances that enhance coherent excitation trapping. These resonances manifest as long-lived ring-down dynamics in the time domain, indicating that the system temporarily stores energy in quasi-stationary Floquet states with suppressed decay, thus prolonging the coherent oscillations observed after the pulse ends.

Figure 13 presents numerical simulations of a driven, interacting four-spin network under a finite-duration pulse. In the experiment, the emitted signal is measured via homodyne detection of the in-phase (I) and quadrature (Q) components, which are proportional to the collective dipole radiation from the system. This output field corresponds to the collective lowering operator  $\sigma_{\text{tot}}^- = \sum_i \sigma_i^-$ , so the measured power reflects the expectation value  $\langle \sigma_{\text{tot}}^+ \sigma_{\text{tot}}^- \rangle$ , directly connecting to the simulated observable  $\langle \sigma^+ \sigma^- \rangle$ . The upper panels show the time-domain evolution of this collective excitation as a function of drive frequency for increasing pulse durations, where pronounced interference patterns emerge in the ring-down following the pulse, as shown in Fig. 13(a). Figure 13(b) displays the corresponding Fourier spectra, which reveal how the spectral content of the ring-down evolves with increasing pulse duration. For short pulses,

the abrupt temporal cutoff introduces large energy uncertainty, resulting in broad sidebands. As the pulse duration increases, the drive becomes more spectrally selective, allowing coherent oscillations among near-resonant modes to build up over time. This temporal coherence leads to narrower sidebands in the Fourier spectrum, which progressively sharpen and approach the bare transition frequencies of the system. This sharpening gives rise to the observed V-shaped structure in the frequency domain that we observe experimentally.

The theoretical framework used here shows good qualitative agreement with the experimental data, capturing key features such as prolonged ring-downs that sharpen with increasing pulse duration, leading to more defined spectral features. This is particularly notable given the general assumptions underlying the model, especially in our TLS framework, where driving is incorporated within the standard tunneling model alongside dipole–dipole interactions. These encouraging results motivate future work aimed at a more detailed theoretical and numerical investigation of the atomistic origin and universal dielectric response of the ensembles of TLS defects probed by our broadband transient spectroscopy technique.

---

[1] R. C. Zeller and R. O. Pohl, Thermal conductivity and specific heat of noncrystalline solids, *Phys. Rev. B* **4**, 2029 (1971).

[2] P. W. Anderson, B. I. Halperin, and C. M. Varma, Anomalous low-temperature thermal properties of glasses and spin glasses, *Philos. Mag.* **25**, 1 (1972).

[3] W. A. Phillips, Tunneling states in amorphous solids, *J. Low Temp. Phys.* **7**, 351 (1972).

[4] W. Arnold and S. Hunklinger, Experimental evidence for the direct interaction between two-level systems in glasses at very low temperatures, *Solid State Commun.* **17**, 883 (1975).

[5] B. Golding and J. E. Graebner, Phonon echoes in glass, *Phys. Rev. Lett.* **37**, 852 (1976).

[6] J. E. Graebner and B. Golding, Phonon echoes in a glass at low temperatures, *Phys. Rev. B* **19**, 964 (1979).

[7] J. L. Black and B. I. Halperin, Spectral diffusion, phonon echoes, and saturation recovery in glasses at low temperatures, *Phys. Rev. B* **16**, 2879 (1977).

[8] P. Hu and L. R. Walker, Spectral diffusion in glasses at low temperatures, *Solid State Commun.* **24**, 813 (1977).

[9] M. Carroll, S. Rosenblatt, P. Jurcevic, I. Lauer, and A. Kandala, Dynamics of superconducting qubit relaxation times, *npj Quantum Inf.* **8**, 132 (2022).

[10] J. H. Béjanin, C. T. Earnest, A. S. Sharafeldin, and M. Mariantoni, Interacting defects generate stochastic fluctuations in superconducting qubits, *Phys. Rev. B* **104**, 094106 (2021).

[11] J. Lisenfeld, C. Müller, J. H. Cole, P. Bushev, A. Lukashenko, and A. V. Ustinov, Electric field spectroscopy of material defects in transmon qubits, *npj Quantum Inf.* **5**, 105 (2019).

[12] C. Wang, C. Axline, Y. Y. Gao, T. Brecht, Y. Chu, L. Frunzio, M. H. Devoret, and R. J. Schoelkopf, Surface participation and dielectric loss in superconducting qubits, *Appl. Phys. Lett.* **107**, 162601 (2015).

[13] A. P. Read, B. J. Chapman, C. U. Lei, J. C. Curtis, S. Ganjam, L. Krayzman, L. Frunzio, and R. J. Schoelkopf, Precision Measurement of the Microwave Dielectric Loss of Sapphire in the Quantum Regime with Parts-per-Billion Sensitivity, *Phys. Rev. Appl.* **19**, 034064 (2023).

[14] D. M. Pozar, *Microwave engineering*, 4th ed. (Wiley, Hoboken, NJ, 2012).

[15] M. D. Reed, B. R. Johnson, A. A. Houck, L. DiCarlo, J. M. Chow, D. I. Schuster, L. Frunzio, and R. J. Schoelkopf, Fast reset and suppressing spontaneous emission of a superconducting qubit, *Appl. Phys. Lett.* **96**, 203110 (2010).

[16] E. M. Purcell, H. C. Torrey, and R. V. Pound, Resonance Absorption by Nuclear Magnetic Moments in a Solid, *Phys. Rev.* **69**, 37 (1946).

[17] J. Lisenfeld, C. Müller, J. H. Cole, P. Bushev, A. Lukashenko, A. Shnirman, and A. V. Ustinov, Measuring the temperature dependence of individual two-level systems by direct coherent control, *Phys. Rev. Lett.* **105**, 230504 (2010).

[18] G. J. Grabovskij, T. Peichl, J. Lisenfeld, G. Weiss, and A. V. Ustinov, Strain tuning of individual atomic tunneling systems detected by a superconducting qubit, *Science* **338**, 232 (2012).

[19] J. Lisenfeld, G. J. Grabovskij, C. Müller, J. H. Cole, G. Weiss, and A. V. Ustinov, Observation of directly interacting coherent two-level systems in an amorphous material, *Nat. Commun.* **6**, 6182 (2015).

[20] L. Yu, S. Matityahu, Y. J. Rosen, C.-C. Hung, A. Maksy-

mov, A. L. Burin, M. Schechter, and K. D. Osborn, Experimentally revealing anomalously large dipoles in the dielectric of a quantum circuit, *Sci. Rep.* **12**, 16960 (2022).

[21] G. S. MacCabe, H. Ren, J. Luo, J. D. Cohen, H. Zhou, A. Sipahigil, M. Mirhosseini, and O. Painter, Nano-acoustic resonator with ultralong phonon lifetime, *Science* **370**, 840 (2020).

[22] K. D. Crowley, R. A. McLellan, A. Dutta, N. Shumiya, A. P. M. Place, X. H. Le, Y. Gang, T. Madhavan, M. P. Bland, R. Chang, N. Khedkar, Y. C. Feng, E. A. Umbarkar, X. Gui, L. V. H. Rodgers, Y. Jia, M. M. Feldman, S. A. Lyon, M. Liu, R. J. Cava, A. A. Houck, and N. P. de Leon, Disentangling losses in tantalum superconducting circuits, *Phys. Rev. X* **13**, 041005 (2023).

[23] P. Chiappina, J. Banker, S. Meesala, D. Lake, S. Wood, and O. Painter, Design of an ultra-low mode volume piezo-optomechanical quantum transducer, *Opt. Express* **31**, 22914 (2023).

[24] M. Chen, J. C. Owens, H. Putterman, M. Schäfer, and O. Painter, Phonon engineering of atomic-scale defects in superconducting quantum circuits, *Sci. Adv.* **10**, eado6240 (2024).

[25] M. P. Bland, F. Bahrami, J. G. C. Martinez, P. H. Prestegard, B. M. Smitham, A. Joshi, E. Hedrick, A. Pakpour-Tabrizi, S. Kumar, A. Jindal, R. D. Chang, A. Yang, G. Cheng, N. Yao, R. J. Cava, N. P. de Leon, and A. A. Houck, 2d transmons with lifetimes and coherence times exceeding 1 millisecond (2025), arXiv:2503.14798 [quant-ph].

[26] J. Gao, M. Daal, A. Vayonakis, S. Kumar, J. Zmuidzinas, B. Sadoulet, B. A. Mazin, P. K. Day, and H. G. Leduc, Experimental evidence for a surface distribution of two-level systems in superconducting lithographed microwave resonators, *Appl. Phys. Lett.* **92**, 152505 (2008).

[27] G. Calusine, A. Melville, W. Woods, R. Das, C. Stull, V. Bolkhovsky, D. Braje, D. Hoyer, D. K. Kim, X. Miloshi, D. Rosenberg, A. Sevi, J. L. Yoder, E. A. Dauler, and W. D. Oliver, Analysis and mitigation of interface losses in trenched superconducting coplanar waveguide resonators, *Appl. Phys. Lett.* **112**, 062601 (2018).

[28] W. Woods, G. Calusine, A. Melville, A. Sevi, E. Golden, D. K. Kim, D. Rosenberg, J. L. Yoder, and W. D. Oliver, Determining interface dielectric losses in superconducting coplanar-waveguide resonators, *Phys. Rev. Appl.* **12**, 014012 (2019).

[29] C. R. H. McRae, H. Wang, J. Gao, M. R. Vissers, T. Brecht, A. Dunsworth, D. P. Pappas, and J. Mutus, Materials loss measurements using superconducting microwave resonators, *Rev. Sci. Instrum.* **91**, 091101 (2020).

[30] C.-C. Hung, L. Yu, N. Foroozani, S. Fritz, D. Gerthsen, and K. D. Osborn, Probing hundreds of individual quantum defects in polycrystalline and amorphous alumina, *Phys. Rev. Appl.* **17**, 034025 (2022).

[31] J. M. Martinis, K. B. Cooper, R. McDermott, M. Steffen, M. Ansmann, K. D. Osborn, K. Cicak, S. Oh, D. P. Pappas, R. W. Simmonds, and C. C. Yu, Decoherence in josephson qubits from dielectric loss, *Phys. Rev. Lett.* **95**, 210503 (2005).

[32] J. Burnett, L. Faoro, I. Wisby, V. L. Gurtovoi, A. V. Chernykh, G. M. Mikhailov, V. A. Tulin, R. Shaikhaidarov, V. Antonov, P. J. Meeson, A. Y. Tzalenchuk, and T. Lindström, Evidence for interacting two-level systems from the 1/f noise of a superconducting resonator, *Nat. Commun.* **5**, 4119 (2014).

[33] C. Müller, J. Lisenfeld, A. Shnirman, and S. Poletto, Interacting two-level defects as sources of fluctuating high-frequency noise in superconducting circuits, *Phys. Rev. B* **92**, 035442 (2015).

[34] A. Agarwal, L. P. Lindoy, D. Lall, F. Jamet, and I. Rungger, Modelling non-markovian noise in driven superconducting qubits, *Quantum Sci. Technol.* **9**, 035017 (2024).

[35] M. Odeh, K. Godeneli, E. Li, R. Tangirala, H. Zhou, X. Zhang, Z.-H. Zhang, and A. Sipahigil, Non-markovian dynamics of a superconducting qubit in a phononic bandgap, *Nat. Phys.* **21**, 406 (2025).

[36] M. Spiecker, A. I. Pavlov, A. Shnirman, and I. M. Pop, Solomon equations for qubit and two-level systems: Insights into non-poissonian quantum jumps, *Phys. Rev. A* **109**, 052218 (2024).

[37] B. R. Mollow, Power spectrum of light scattered by two-level systems, *Phys. Rev.* **188**, 1969 (1969).

[38] C. Macklin, K. O'Brien, D. Hoyer, M. E. Schwartz, V. Bolkhovsky, X. Zhang, W. D. Oliver, and I. Siddiqi, A near-quantum-limited josephson traveling-wave parametric amplifier, *Science* **350**, 307 (2015).

[39] K. O'Brien, C. Macklin, I. Siddiqi, and X. Zhang, Resonant phase matching of josephson junction traveling wave parametric amplifiers, *Phys. Rev. Lett.* **113**, 157001 (2014).

[40] M. Boselli, J. Grebel, A. Peugeot, R. Dassonneville, B. Huard, and A. Bienfait, Observation and mitigation of microwave echoes from dielectric defects in josephson traveling wave amplifiers (2025), arXiv:2503.00190 [quant-ph].

[41] A. Delattre, I. Golokolenov, R. Pedurand, N. Roch, A. Ranadive, M. Esposito, L. Planat, A. Fefferman, E. Collin, X. Zhou, M. A. Sillanpää, L. Mercier de Lepinay, A. D. Armour, and J. Glathard, Quantitative calibration of a TWPA applied to an optomechanical platform (2025), arXiv:2505.05837 [quant-ph].

[42] A. M. Holder, K. D. Osborn, C. J. Lobb, and C. B. Musgrave, Bulk and surface tunneling hydrogen defects in alumina, *Phys. Rev. Lett.* **111**, 065901 (2013).

[43] A. Megrant and Y. Chen, Scaling up superconducting quantum computers, *Nature Electronics* , 1 (2025).

[44] M. Thorwart, M. Grifoni, and P. Hänggi, Strong coupling theory for driven tunneling and vibrational relaxation, *Phys. Rev. Lett.* **85**, 860 (2000).

[45] R. Kubo, Statistical-Mechanical Theory of Irreversible Processes. I. General Theory and Simple Applications to Magnetic and Conduction Problems, *J. Phys. Soc. Jpn.* **12**, 570 (1957).

[46] C. W. Gardiner and M. J. Collett, Input and output in damped quantum systems: Quantum stochastic differential equations and the master equation, *Phys. Rev. A* **31**, 3761 (1985).

[47] L. Novotny, M. Frimmer, A. Militaru, A. Norrman, O. Romero-Isart, and P. Maurer, Optomechanical sideband asymmetry explained by stochastic electrodynamics, *Phys. Rev. A* **106**, 043511 (2022).

[48] L. Stefanazzi, K. Treptow, N. Wilcer, C. Stoughton, C. Bradford, S. Uemura, S. Zorzetti, S. Montella, G. Cancelo, S. Sussman, A. Houck, S. Saxena, H. Arnaldi, A. Agrawal, H. Zhang, C. Ding, and D. I. Schuster, The qick (quantum instrumentation control kit): Readout and control for qubits and detectors, *Rev. Sci. Instrum.*

**93**, 044709 (2022).

[49] K. D. Crowley, R. A. McLellan, A. Dutta, N. Shumiya, A. P. M. Place, X. H. Le, Y. Gang, T. Madhavan, M. P. Bland, R. Chang, N. Khedkar, Y. C. Feng, E. A. Umbarkar, X. Gui, L. V. H. Rodgers, Y. Jia, M. M. Feldman, S. A. Lyon, M. Liu, R. J. Cava, A. A. Houck, and N. P. De Leon, Disentangling Losses in Tantalum Superconducting Circuits, *Phys. Rev. X* **13**, 041005 (2023).

[50] J. Lisenfeld, C. Müller, J. H. Cole, P. Bushev, A. Lukashenko, A. Shnirman, and A. V. Ustinov, Measuring the Temperature Dependence of Individual Two-Level Systems by Direct Coherent Control, *Phys. Rev. Lett.* **105**, 230504 (2010).

[51] A. P. M. Place, L. V. H. Rodgers, P. Mundada, B. M. Smitham, M. Fitzpatrick, Z. Leng, A. Premkumar, J. Bryon, A. Vrajitoarea, S. Sussman, G. Cheng, T. Madhavan, H. K. Babla, X. H. Le, Y. Gang, B. Jäck, A. Gynnis, N. Yao, R. J. Cava, N. P. de Leon, and A. A. Houck, New material platform for superconducting transmon qubits with coherence times exceeding 0.3 milliseconds, *Nat. Commun.* **12**, 1779 (2021).

[52] S. Sangtawesin, B. L. Dwyer, S. Srinivasan, J. J. Allred, L. V. H. Rodgers, K. De Greve, A. Stacey, N. Dontschuk, K. M. O'Donnell, D. Hu, D. A. Evans, C. Jaye, D. A. Fischer, M. L. Markham, D. J. Twitchen, H. Park, M. D. Lukin, and N. P. de Leon, Origins of diamond surface noise probed by correlating single-spin measurements with surface spectroscopy, *Phys. Rev. X* **9**, 031052 (2019).

[53] M. W. Olszewski, J. T. Paustian, T. Banerjee, H. Lu, J. L. Ramirez, N. Nguyen, K. Okubo, R. Pant, A. B. Biedron, D. C. Ralph, C. J. K. Richardson, G. D. Fuchs, C. R. H. McRae, I. V. Pechenezhskiy, B. L. T. Plourde, and V. Fatemi, Low-loss nb on si superconducting resonators from a dual-use spintronics deposition chamber and with acid-free post-processing (2025), arXiv:2503.13285 [quant-ph].

[54] C. Gaikwad, D. Kowsari, C. Brame, X. Song, H. Zhang, M. Esposito, A. Ranadive, G. Cappelli, N. Roch, E. M. Levenson-Falk, and K. W. Murch, Entanglement assisted probe of the non-markovian to markovian transition in open quantum system dynamics, *Phys. Rev. Lett.* **132**, 200401 (2024).

[55] R. D. Chang, N. Shumiya, R. A. McLellan, Y. Zhang, M. P. Bland, F. Bahrami, J. Mun, C. Zhou, K. Kisslinger, G. Cheng, B. M. Smitham, A. C. Pakpour-Tabrizi, N. Yao, Y. Zhu, M. Liu, R. J. Cava, S. Gopalakrishnan, A. A. Houck, and N. P. de Leon, Eliminating surface oxides of superconducting circuits with noble metal encapsulation, *Phys. Rev. Lett.* **134**, 097001 (2025).

[56] C. M. Quintana, A. Megrant, Z. Chen, A. Dunsworth, B. Chiaro, R. Barends, J. Kelly, J. Mutus, D. Sank, J. Wenner, Y. Yin, J. Zhao, A. N. Cleland, and J. M. Martinis, Characterization and reduction of microfabrication-induced decoherence in superconducting quantum circuits, *Appl. Phys. Lett.* **105**, 062601 (2014).

[57] C. Müller, J. H. Cole, and J. Lisenfeld, Towards understanding two-level-systems in amorphous solids: insights from quantum circuits, *Rep. Prog. Phys.* **82**, 124501 (2019).

[58] B. Lévi, C. C. López, J. Emerson, and D. G. Cory, Efficient error characterization in quantum information processing, *Phys. Rev. A* **75**, 022314 (2007).

[59] E.-M. Laine, J. Piilo, and H.-P. Breuer, Measure for the non-markovianity of quantum processes, *Phys. Rev. A* **81**, 062115 (2010).

[60] A. Rivas, S. F. Huelga, and M. B. Plenio, Measures of non-markovianity: Divisibility versus backflow of information, *Phys. Rev. A* **83**, 052128 (2011).

[61] M. S. Kumar and G. S. Agarwal, Effects of arbitrary relaxation and strong-field dressing of energy levels on nonlinear optical susceptibilities, *Phys. Rev. A* **33**, 1817 (1986).

[62] M. M. Ali, P.-Y. Lo, M. W.-Y. Tu, and W.-M. Zhang, Non-markovianity measure using two-time correlation functions, *Phys. Rev. A* **92**, 062306 (2015).

[63] G. Busiello, Out-of-equilibrium dissipative ac-susceptibility in quantum ising spin glass, *J. Mod. Phys.* **04**, 784 (2013).

[64] F. Castles, J. A. J. Fells, D. Isakov, S. M. Morris, A. A. R. Watt, and P. S. Grant, Active metamaterials with negative static electric susceptibility, *Adv. Mater.* **32**, 1904863 (2020).

[65] B. M. Terhal and G. Burkard, Fault-tolerant quantum computation for local non-markovian noise, *Phys. Rev. A* **71**, 012336 (2005).

[66] P. W. Shor, Fault-tolerant quantum computation, in *Proceedings of the 37th Annual Symposium on Foundations of Computer Science (FOCS)* (1996) pp. 56–65.

[67] Z.-H. Zhang, K. Godeneli, J. He, M. Odeh, H. Zhou, S. Meesala, and A. Sipahigil, Acceptor-induced bulk dielectric loss in superconducting circuits on silicon, *Phys. Rev. X* **14**, 041022 (2024).

[68] Y. Shalibo, Y. Rofe, D. Shwa, F. Zeides, M. Neeley, J. M. Martinis, and N. Katz, Lifetime and coherence of two-level defects in a josephson junction, *Phys. Rev. Lett.* **105**, 177001 (2010).

[69] A. K. Jonscher, The 'universal' dielectric response, *Nature* **267**, 673 (1977).

[70] A. Jonscher, The universal dielectric response and its physical significance, *IEEE Trans. Electr. Insul.* **27**, 407 (1992).

[71] L. Stefanazzi, K. Treptow, N. Wilcer, C. Stoughton, C. Bradford, S. Uemura, S. Zorzetti, S. Montella, G. Cancelo, S. Sussman, A. Houck, S. Saxena, H. Arnaldi, A. Agrawal, H. Zhang, C. Ding, and D. I. Schuster, The QICK (Quantum Instrumentation Control Kit): Readout and control for qubits and detectors, *Rev. Sci. Instrum.* **93**, 044709 (2022).

[72] U. D. Giovannini and H. Hübener, Floquet analysis of excitations in materials, *Journal of Physics: Materials* **3**, 012001 (2019).

[73] M. Grifoni and P. Hänggi, Driven quantum tunneling, *Physics Reports* **304**, 229 (1998).